Journal of the Meteorological Society of Japan, **97**(1), 191−203, 2019. doi:10.2151/jmsj.2019-011
Special Edition on Tropical Cyclones in 2015−2016

An Evaluation of COAMPS-TC Real-Time Forecasts for Super Typhoon Nepartak (2016)

Hao JIN, Yi JIN, and James D. DOYLE

Naval Research Laboratory, California, USA

(Manuscript received 3 April 2018, in final form 25 October 2018)

Abstract

Typhoon Nepartak was a category 5 tropical cyclone in 2016 that resulted in significant societal impacts. The tropical cyclone went through a rapid intensification (RI), with an increase of maximum wind speed of 51 m s^{-1} and a decrease of minimum sea level pressure of 74 hPa in 42 h. The real-time forecast from the U.S. Navy Coupled Ocean/Atmosphere Mesoscale Prediction System – Tropical Cyclone (COAMPS-TC), initialized at 1200 UTC 3 July, predicted the track and intensity reasonably well for Super Typhoon Nepartak and captured the storm's RI process. Positive interactions among primary and secondary circulations, surface enthalpy fluxes, and mid-level convective heating are demonstrated to be critical for the RI. The storm structure variations seen from the simulated satellite infrared brightness temperature during RI bear considerable resemblance to the Himawari-8 satellite images, although the forecast inner core is too broad, presumably due to the relatively coarse resolution (5 km) used for the real-time forecasts at the time.

Keywords tropical cyclone; typhoon; rapid intensification

Citation Jin, H., Y. Jin, and J. D. Doyle, 2019: An evaluation of COAMPS-TC real-time forecasts for Super Typhoon Nepartak (2016). *J. Meteor. Soc. Japan*, **97**, 191–203, doi:10.2151/jmsj.2019-011.

1. Introduction

Super Typhoon Nepartak was the first category 5 (over 70 m s^{-1} or 136 kt on the Saffir-Simpson hurricane wind scale) tropical cyclone of 2016 and had significant societal impacts with over $1.8B (USD) of damage (ESCAP/WMO Typhoon Committee 2017). It formed as a tropical depression on July 2 near Guam in the western Pacific Ocean and strengthened to a tropical storm the following day. Rapid intensification ensued with a decrease in minimum sea-level pressure (MSLP) from 985 hPa at 1200 UTC 4 July to 911 hPa at 0600 UTC July 6, and a concurrent increase in maximum wind speed of 100 kt (51.4 m s^{-1}) during this same period, followed by a secondary eyewall formation and eyewall replacement cycle, before making landfall in Taiwan. The storm impacted Taiwan with 135 kt (69.4 m s^{-1}) sustained winds and heavy precipitation, resulting in 3 deaths and substantial damage in Taiwan (Central Emergency Operation Center 2016). It made a second landfall in Fujian, China, on July 9 with 65 kt (33.4 m s^{-1}) wind speed, causing more than 111 deaths and over $1.5B (USD) of damage (China News Service 2016), and the most devastating flooding since 1998. The rapid changes in the intensity of Super Typhoon Nepartak presented a major challenge for operational tropical cyclone prediction models, which failed in general to capture Nepartak's intensity changes.

While TC intensification is challenging enough to predict, rapid intensification (RI) is even more challenging due to its sudden onset and rapid evolution.

Corresponding author: Hao Jin, Naval Research Laboratory, 7 Grace Hopper Ave., Monterey, CA 93943, USA
E-mail: hao.jin@nrlmry.navy.mil
J-stage Advance Published Date: 12 November 2018

Holiday and Thompson (1979) defined RI as a decrease of the MSLP greater than 42 hPa day^{-1}. Kaplan and DeMaria (2003) added another criterion: surface maximum wind speed (MWS) increase of more than 15.4 m s^{-1} (30 kt) over a 24-h period. Various dynamic and thermodynamic processes are believed to play important roles in TC intensification. Emanuel (1986, 1994, 2003) proposed the wind-induced surface heat exchange (WISHE) mechanism to explain the positive interaction between the near-surface wind speed and the surface enthalpy fluxes from the underlying ocean during intensification. The various paradigms of TC intensification have been reviewed by Montgomery and Smith (2014), in which the authors argued for a more consistent treatment of both dynamic and thermodynamic processes.

The high-resolution real-time forecasts from the Coupled Ocean/Atmosphere Mesoscale Prediction System–Tropical Cyclone (COAMPS-TC, a registered trademark of the US Naval Research Laboratory, Doyle et al. 2014) are examined here for Nepartak's RI process. The objectives of this study are to: (i) evaluate real-time track and intensity forecast for Typhoon Nepartak; (ii) assess and understand the key processes occurring during RI from an azimuthally averaged perspective; (iii) document the positive interactions among the primary and secondary circulations, the convective latent heat release, and surface heat fluxes during the RI period; and (iv) evaluate Nepartak's structure during RI through a comparison of model-simulated synthetic brightness temperature (TB) with high-frequency satellite observations from the geostationary satellite Himawari-8 operated by the Japan Meteorological Agency (JMA).

2. Model description and initialization

The COAMPS-TC system, developed by the Naval Research Laboratory (NRL) (Doyle et al. 2014), is used in this study. The Kain-Fritsch cumulus parameterization is used for grid spacing at 9-km or larger and a modified bulk microphysics parameterization based on Rutledge and Hobbs (1984) is applied in all domains. The planetary boundary layer turbulent mixing scheme is based on a modified 1.5 order Mellor-Yamada scheme (Mellor and Yamada 1974). A mixing length formulation following Bougeault and Lacarrère (1989), a dissipative heating parameterization (Jin et al. 2007), and Fu-Liou radiation scheme (Fu and Liou 1993; Liu et al. 2009) are used in this real-time application of COAMPS-TC. In COAMPS-TC, the roughness length for momentum is modified to allow the momentum exchange coefficient to level off at wind speeds greater than 25 m s^{-1}, which is based on observations and theory from Donelan et al. (2004), and then the drag decreases with increasing intensity beyond ~ 30 m s^{-1} (Soloviev et al. 2014). The Geophysical Fluid Dynamics Laboratory (GFDL) tracker (Marchok 2002) is used to determine the storm track and intensity.

The configuration for the operational forecasts in 2016 includes one fixed coarse mesh with 45-km grid spacing and two two-way interactive moving nests that follow the storm with 15-km and 5-km grid spacing, respectively (blue boxes in Fig. 1). The vertical domain consists of 40 terrain-following coordinate levels, extending from 10 m above the surface to a model top at approximately 32 km. The initial and boundary conditions consist of the forecasts (at 0.5-degree resolution) produced by the Global Forecast System (GFS) from the National Centers for Environmental Prediction (NCEP).

3. Track and intensity forecast

The COAMPS-TC track forecast for Typhoon Nepartak agrees with the best track from Joint Typhoon Warning Center (JTWC) reasonably well for the forecast starting from 1200 UTC 3 July 2016 (Fig. 2). For forecasts initialized at later times, a rightward bias is apparent in some of COAMPS-TC forecasts, which is not inconsistent with other operational models (https://www.nrlmry.navy.mil/coamps-web/web/tc?sid=02W&ddtg=2016070312&scl=4). COAMPS-TC predicts the slow movement of Typhoon Nepartak and the timing of landfall reasonably well, with a ~ 6–12 h delay. The limitations in current operational tropical cyclone forecasts may be contributed by uncertainty of both large- and small-scale environment and their interaction, along with a lack of observations at small scales to better initialize the vortex. The landfall location is close to the estimated landfall location near southern Taiwan.

The COAMPS-TC captures the rapid intensification of Typhoon Nepartak. The forecast MSLP decreases from 980 hPa at 42 h to 897 hPa at 90 h, an 83 hPa decrease in 48 h (Fig. 3a), compared to 78 hPa observed decrease (from 989 hPa at 18 h to 911 hPa at 66 h). The MWS increases from ~ 36 m s^{-1} to ~ 78 m s^{-1} (during 42–90 h) an increase of 42 m s^{-1} compared to an observed 53 m s^{-1} increase (from 23 m s^{-1} at 18 h to about 76 m s^{-1} at 66 h). The COAMPS-TC performed relatively better than other operational models with regard to Nepartak's RI at this forecast time (Fig. 3).

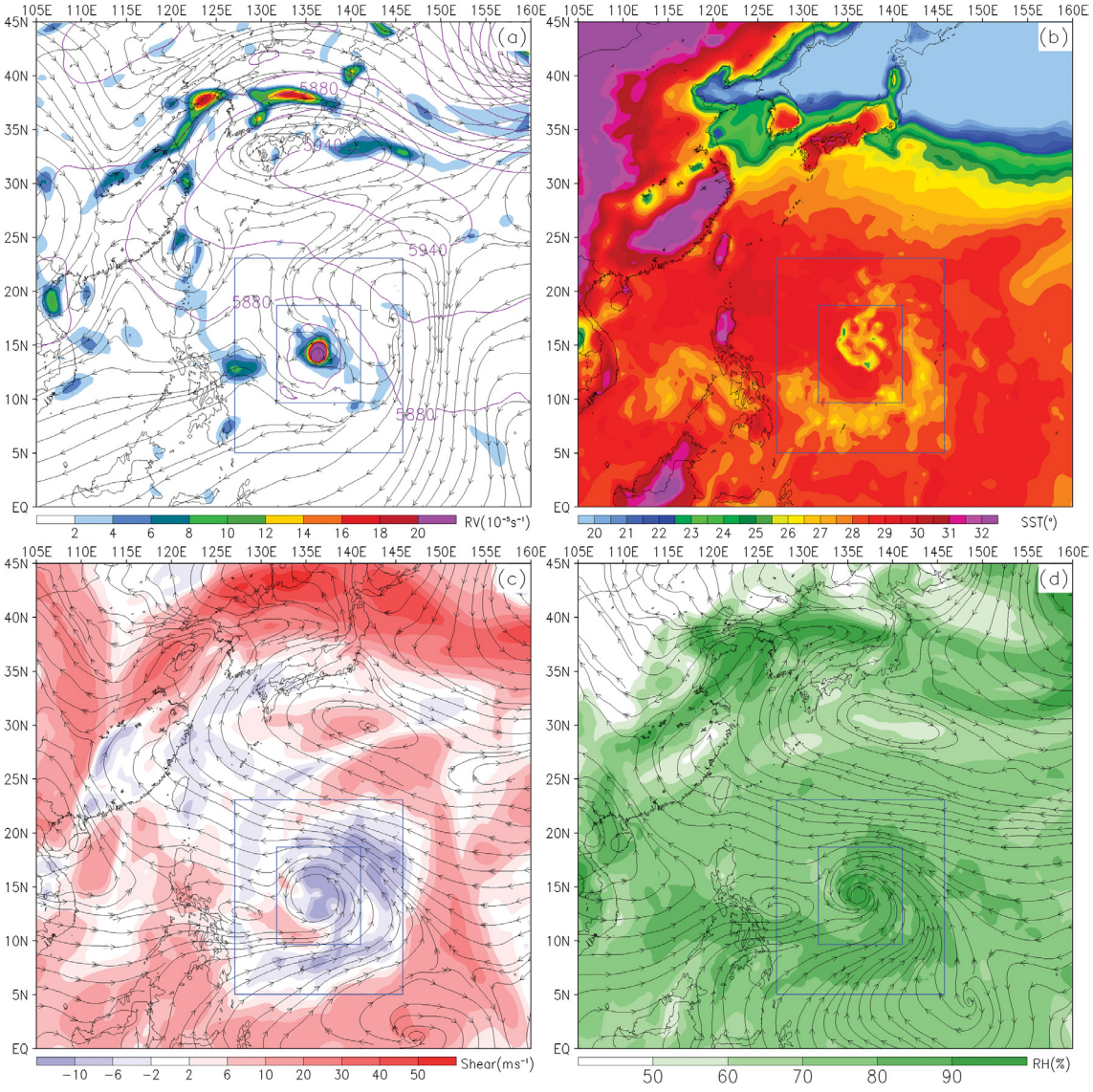

Fig. 1. (a) 850-hPa relative vorticity (shaded, 10^{-5} s^{-1}), 500-hPa geopotential height (purple contours, m) and 200-hPa winds (stream), (b) sea surface temperature (0°C), (c) 200–850 hPa wind shear (shaded, m s^{-1}) and 850-hPa winds (stream), and (d) surface to 850-hPa averaged relative humidity (%) and winds (stream) from model domain 1 with 45 km horizontal grid spacing at 42-h model time, (valid at 0600 UTC 5 July 2016), just before the RI. The blue boxes are the two nested domains with grid spacing of 15-, and 5- km centered at Typhoon Nepartak and moving along with the storm.

4. Rapid intensification

Figure 1 shows the large-scale environment at 42-h (the starting time for the simulated RI, as shown Fig. 3a) from the forecast initialized at 1200 UTC 3 July 2016, when Typhoon Nepartak is located south of Guam in the western Pacific Ocean. Nepartak has an intense core of 850-hPa relative vorticity with a maximum of 2×10^{-4} s^{-1} and strong upper level divergence at 200 hPa (Fig. 1a). A subtropical high is located to the north of the system, as shown from 500-hPa geopotential height distribution, acting as a dominant forcing for the steering flow. The sea surface temperature (SST) in the western Pacific Ocean along the

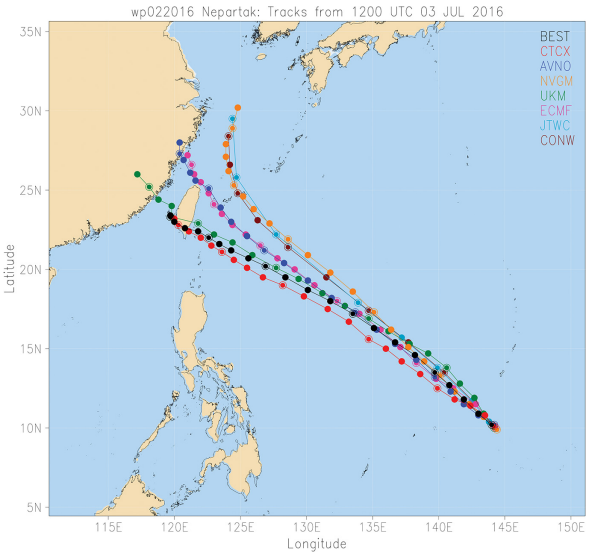

Fig. 2. Comparison of multi-model real-time track forecasts initialized at 1200 UTC 3 July 2016 with the best-track (black) for Typhoon Nepartak. CTCX (red) is the COAMPS-TC forecast track. The dots correspond to the storm locations every 6-h.

northwesterly storm path towards Taiwan is relatively warm (above 30°C) (Fig. 1b). Vertical wind shear between 850 and 200 hPa is moderate (~ 10 m s^{-1}) along the storm path (Fig. 1c), with 850-hPa winds from the southwest and 200-hPa winds from the northeast. The storm develops in a rich moisture environment, with the averaged relative humidity (from surface to 850 hPa) over 90 % within the inner-core of the storm (Fig. 1d). The moisture in the vicinity of the storm is primarily transported by the prominent southwesterly low-level flow. The warmer SSTs, rich low-level moisture, low-level convergence, and upper-level divergence over the TC, provide a favorable large-scale environment for the RI, which agrees with the previous studies on the environmental conditions of TC intensification and RI (Merrill 1988; Kaplan et al. 2010).

Figure 4 depicts the evolution of azimuthally-averaged tangential and radial winds and vertical velocity during the RI period. The storm is relatively weak at 48 h with the peak tangential wind speed at ~ 40 m s^{-1} and the peak radial inflow at ~ 5 m s^{-1} (Fig. 4a). The storm then intensifies with the peak tangential wind over 50 m s^{-1} and the peak radial inflow increase to 10 m s^{-1} (Fig. 4b). The 40 m s^{-1} contour of the primary circulation extends from 3 km at 48 h to 5 km at 60 h. The peak tangential wind rapidly increases to 60 m s^{-1} and the peak radial wind increases to 20 m s^{-1} by 72 h with the 40 m s^{-1} contour extending through a deep layer up to ~ 12 km (Fig. 4c). The surface inflow layer depth increases from ~ 500 m to ~ 1-km near the eyewall as the radius of maximum wind (RMW) increase. The peak vertical velocity reaches over 2.5 m s^{-1} at 12-km height. Both the tangential winds (the primary circulation) and radial winds connected through vertical velocity (the secondary circulation)

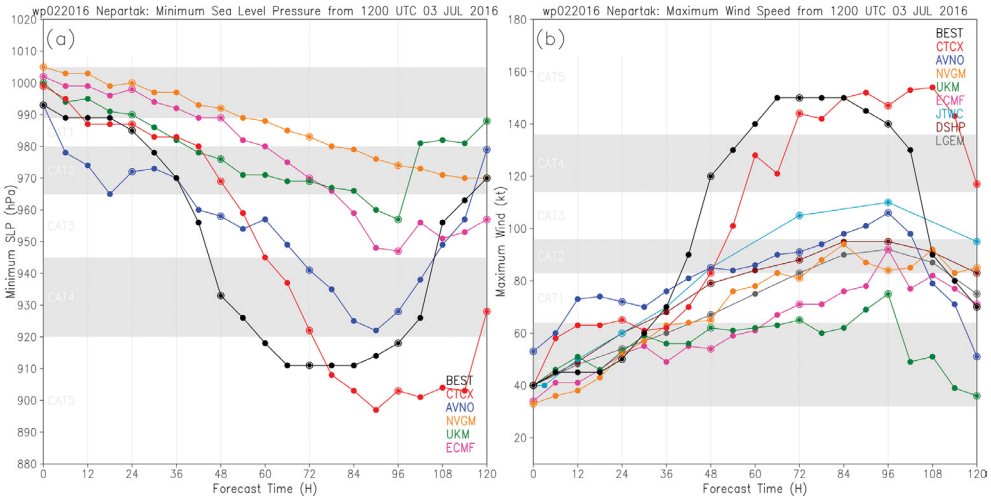

Fig. 3. Comparison of multi-model real-time intensity forecasts initialized at 1200 UTC 3 July 2016 with the best-track (black) for Typhoon Nepartak: (a) minimum sea level pressure (hPa) and (b) maximum wind speed (kt, 1 kt = 0.51444 m s^{-1}).

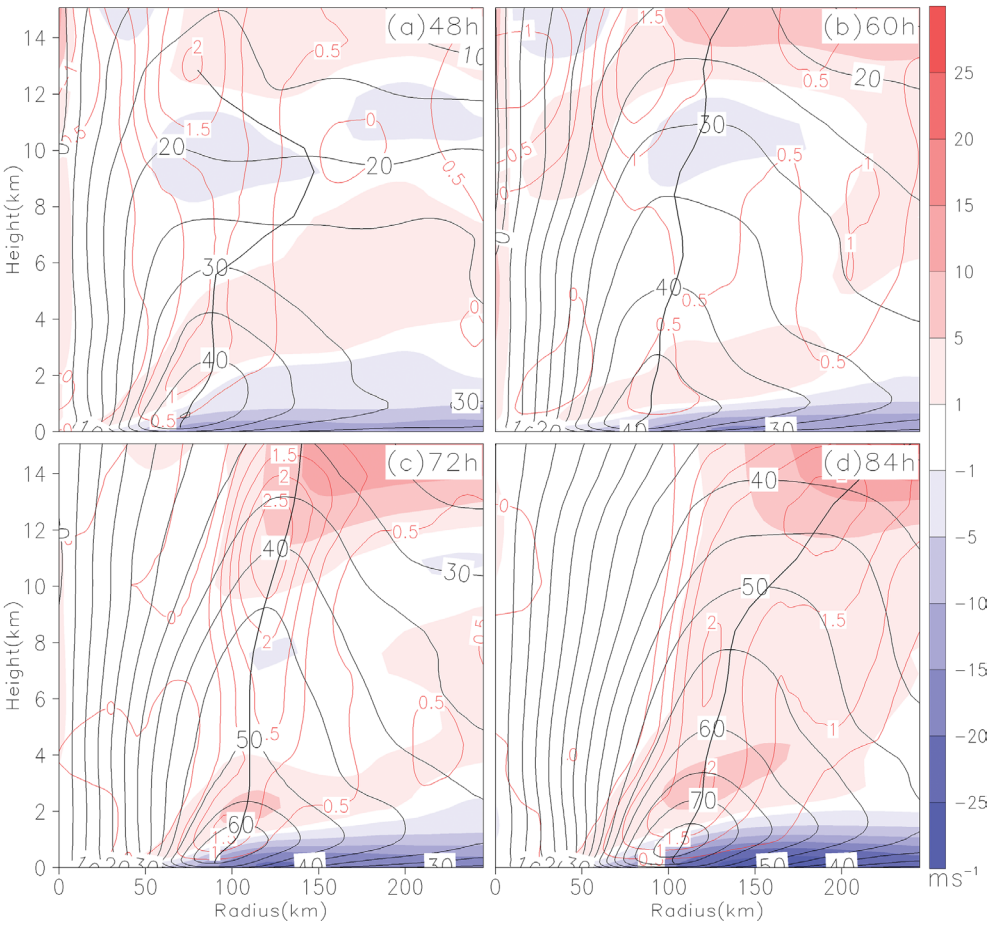

Fig. 4. Radius-height plots of the azimuthally averaged radial winds (shaded, m s^{-1}), tangential winds (black contours, m s^{-1}), vertical velocity (red contours at 0.5 m s^{-1} intervals), and the radius of maximum winds (RMW, black line) at (a) 48 h, (b) 60 h, (c) 72 h, and (d) 84 h.

become significantly enhanced and much better organized. The storm's tangential winds reach the maximum value of 75 m s^{-1} by 84 h with the 40 m s^{-1} contour extending upward to a 14-km altitude (Fig. 4d). The peak radial inflow increases to 25 m s^{-1} and the thickness of the radial inflow layer extends vertically to ~ 1.5 km. The storm size (measured by RMW) is ~ 60–80 km during the RI period, relatively large compared to other storms that went through RI (e.g., Stern et al. 2015).

It is well established by previous studies that warmer SSTs are correlated with TCs that undergo RI. Although Kanada et al. (2017) suggested that the RI is sensitive to the SST pattern, the SST at the storm center is used here as a basic and more independent (of storm size) diagnostic. Figure 5 shows time series of SST and the value of 200–850-hPa vertical wind shear at the storm center following with the storm movement along the forecast time. The SST is warm (> 29.4°C) and exceeds 30°C during the RI period (42–90 h). The vertical wind shear is ~ 7 m s^{-1} at 42 h and decreases to ~ 3 m s^{-1} between 54–72 h. The vertical shear increases from 4 m s^{-1} at 78 h to ~ 8 m s^{-1} by 90 h. This analysis suggests that the increasingly warm SSTs and the low vertical wind shear during the period of 54–78 h provide favorable environmental conditions for RI.

Figure 6 provides a more detailed depiction of the interaction between the primary and secondary circulations in the typhoon boundary layer during the RI (60–78 h). The low-level radial inflow increases from ~ 15 m s^{-1} to ~ 20 m s^{-1} and expands vertically, along with an increase of tangential wind speed (primary circulation) from 40 m s^{-1} to 70 m s^{-1}. Associated with

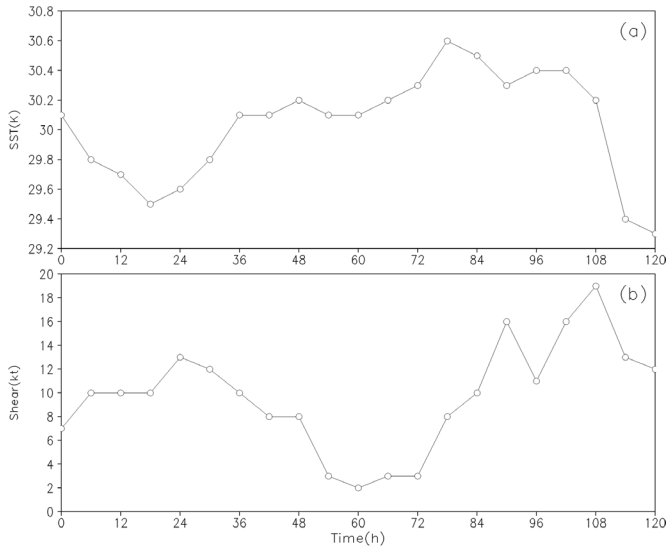

Fig. 5. Time series of model output (circles) (a) SST and (b) the value of 850–200 hPa vertical wind shear (kt, 1 kt = 0.514 m s^{-1}) at the storm center.

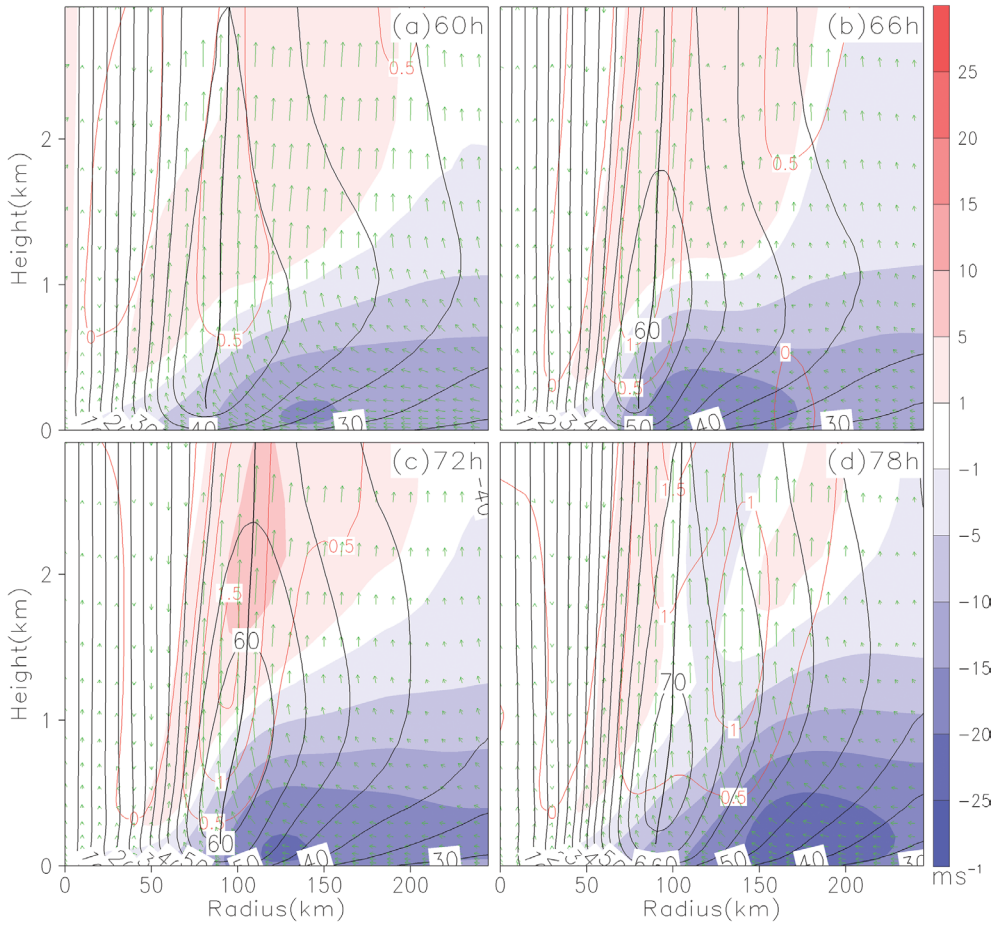

Fig. 6. Vertical zoomed-in radius-height plots of the azimuthally averaged radial winds (shaded, m s^{-1}), tangential winds (black contours, m s^{-1}), vertical velocity (red contours, m s^{-1}), wind vectors (green, expanded vertically with vertical-horizontal ratio) and RMW (black line) at (a) 60 h, (b) 66 h, (c) 72 h, and (d) 78 h.

the enhanced radial inflow, the upward motion also intensifies along the eyewall, as shown by the green vectors, which reflects the positive interactions between the primary and secondary circulations during RI from a kinematic perspective.

At 60 h two diabatic heating centers begin to form, with one at the lower levels (below 4-km) and a second at mid- to upper-levels (6–12 km), separated by a diabatic cooling region near the melting layer at 4–6 km (Fig. 7a). The mid- to upper-level diabatic heating rapidly increases and exceeds 150 K h^{-1} at 66 h; this occurs at a much faster rate than that at the lower levels (~ 100 K h^{-1}), in part due to the larger ascent in the mid- to upper-levels (Fig. 7b). Over the next 12 h, the eyewall updraft continues to intensify and at the same time the diabatically-induced cooling is reduced and moves outward from the eyewall (Figs. 7c, d). A warm core (up to +10°C) has been well established at mid- to upper-levels.

The surface enthalpy fluxes beneath the typhoon eyewall increase moderately over the first 2 days of the simulation, reaching 800 W m^{-2} for the azimuthally averaged value at 48 h (Fig. 8a), at the onset of RI. The enthalpy fluxes increase rapidly during RI and reach 2000 W m^{-2} by 84 h, associated with the increase in the tangential wind (i.e., the primary circulation) from 30 m s^{-1} to 60 m s^{-1}. During the 42–84 h period, the radial wind (i.e., the secondary circulation) increases from 6 m s^{-1} to 24 m s^{-1} along with a 1-km vertical velocity increase from 0.5 to 1.5 m s^{-1} (Fig. 8b). The diabatic heating and vertical velocity at 8-km height increase greatly during the 42–84 h period (Fig. 8c). It is noteworthy that the increase in the upper-level vertical velocity is larger (particularly during the

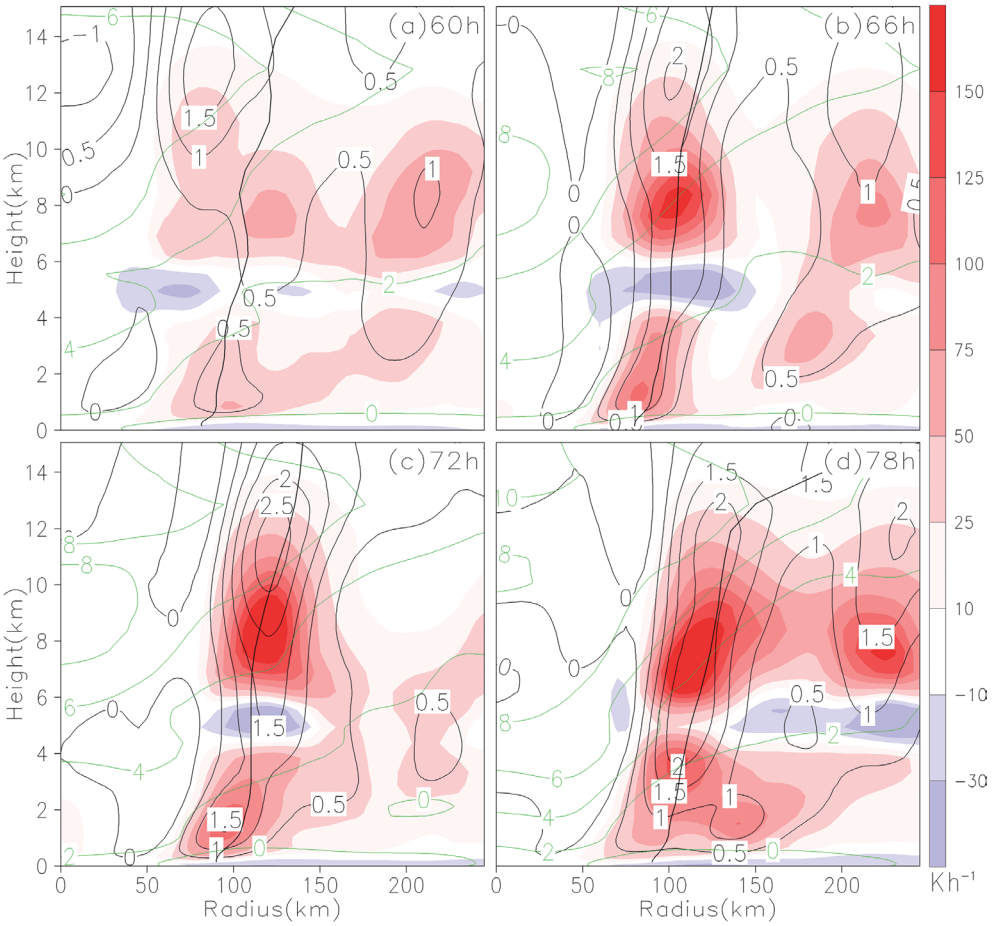

Fig. 7. Radius-height plots of the azimuthally averaged diabatic heating rate (shaded, K h^{-1}), vertical velocity (back contours, m s^{-1}), temperature anomaly (from the domain average temperature, green contours, K), and RMW (black line) at (a) 60 h, (b) 60 h, (c) 72 h, and (d) 78 h.

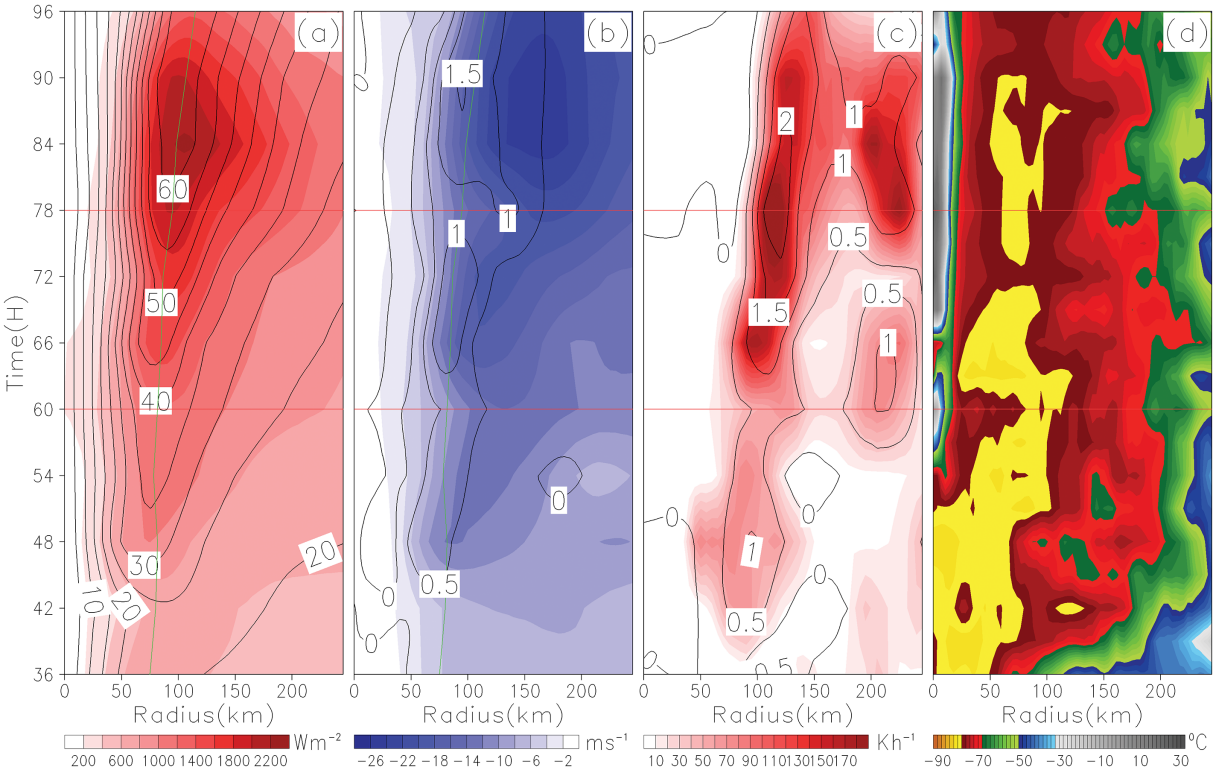

Fig. 8. Radius-time plots of the azimuthally averaged (a) surface enthalpy heat flux (shaded, W m^{-2}), 10-m tangential wind (black contours, m s^{-1}) and the RMW (green line, defined as the radius of maximum 10-m winds from storm center to 250 km); (b) 10-m radial wind (shaded, m s^{-1}), 1-km height vertical velocity (black contours, m s^{-1}), and the RMW (green line); (c) 8-km height diabatic heating rate (shaded, K h^{-1}) and 8-km vertical velocity (black contours, m s^{-1}); (d) brightness temperature (shade, °C) from the 36- to 96-h simulations. The period between red lines are an example of positive interactions between primary, secondary circulations, enthalpy flux, and diabatic heating.

60–78 h period) relative to the lower level vertical velocity during RI, in part due to the strong interactions between the vertical velocity and diabatic heating. The TB at the cloud top (less −80°C) suggests that the deep convection is very active within the eyewall during the early portion of the RI (36–60 h) (Fig. 8d). The convective cloud structure undergoes reorganization during 60–69 h and takes on a more asymmetric appearance (Figs. 11f–i) with a smaller area of low TB (less than −80°C). The higher TB in the eye is consistent with the clear eye structure apparent as the storm intensifies during 54–90 h.

During the 60–78 h period (two red lines in Fig. 9 delineating the starting and ending times of the positive interactions during the RI), a noticeable increase in both the primary circulation (Fig. 9a) and secondary circulation (Fig. 9b) are closely related to increased surface enthalpy fluxes (Fig. 9c), consistent with previous studies (Emanuel 1986; Kondo 1975). The intensified secondary circulation provides low-level moist air that is entrained into the eyewall that leads to stronger ascent (Fig. 9d) and latent heat release (Fig. 9e), which further reinforces the secondary circulation (Fig. 5).

The evolution of the structure of Typhoon Nepartak is apparent in the satellite observations derived from Himawari-8 (Fig. 10). The vigorous deep convection within the inner-core region of the TC is apparent from the high cloud tops that attain a TB < −80°C. The TC was not well organized at 0300 UTC 5 July and exhibited an asymmetric inner core (deepest convection located to the south of the eye) and bands of convection located to the north and northeast (Fig. 10a). The TC became more organized with a tightly structured inner core by 0710 UTC 5 July, however it retained an asymmetric appearance with enhanced

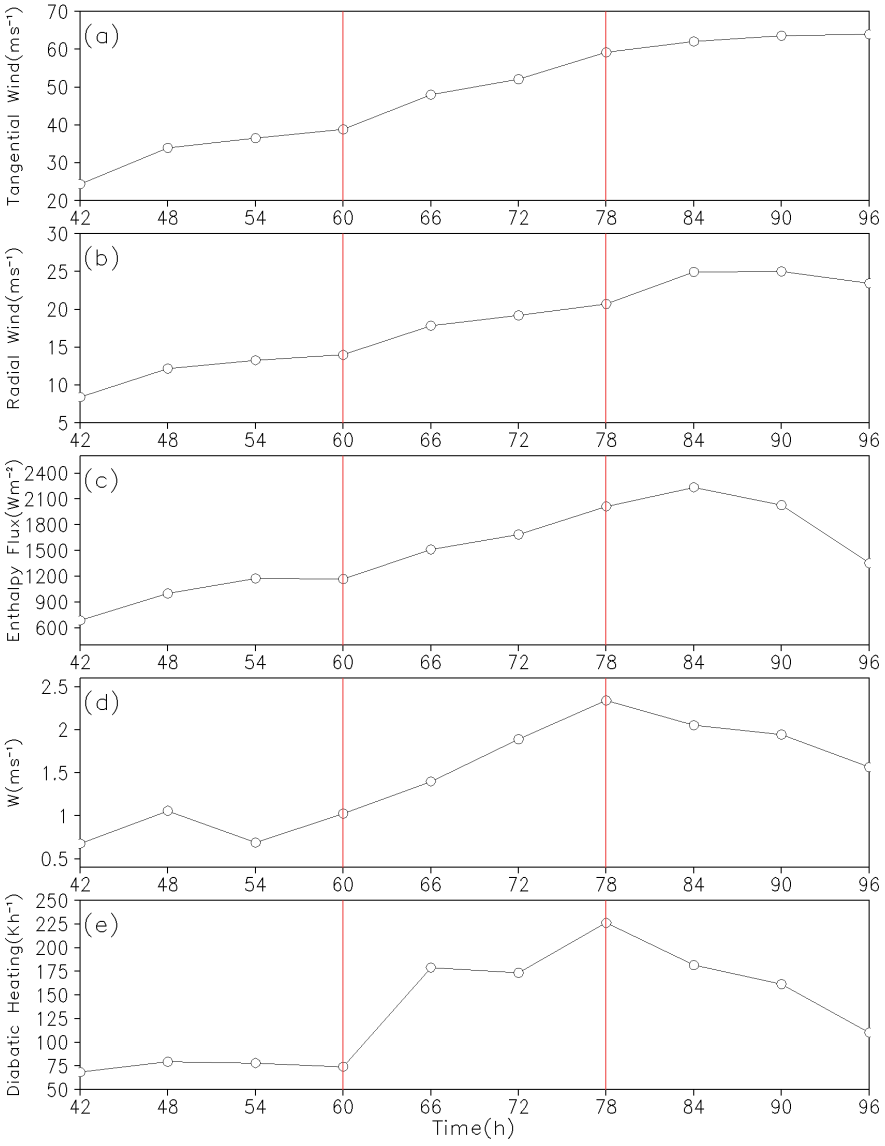

Fig. 9. Time series of the maximum values of the azimuthally averaged (a) 10-m tangential wind (m s^{-1}), (b) 10-m radial wind (m s^{-1}), (c) surface enthalpy flux (W m^{-2}), (d) 8-km vertical velocity (m s^{-1}), and (e) 8-km diabatic heating rate (K h^{-1}) from the typhoon center. The period between red lines highlight positive interactions between the primary, secondary circulations, enthalpy flux, and diabatic heating.

convection in the southern semi-circle (Fig. 10b). As the TC strengthened further to its peak intensity, a small eye with a radius of ~10 km was clearly apparent (Figs. 10c–f). During the weakening stage, the deep convection region was reduced in size and became more prominent in the southern semi-circle as the storm structure attained more asymmetric structure (Figs. 10g–i).

To evaluate the real-time forecast using the satellite observations, we computed synthetic TB (Bikos et al. 2012) for the COAMPS-TC forecasts following Jin et al. (2014). The model forecast hydrometeors (cloud droplets, rain, ice, snow, and graupel) and thermodynamic fields (e.g., pressure, temperature, and humidity) are used as input for a forward radiative transfer model to derive a synthetic TB analogous to the satellite observations. The simulated TBs displayed in Fig. 11 are at the similar locations and intensity relative to

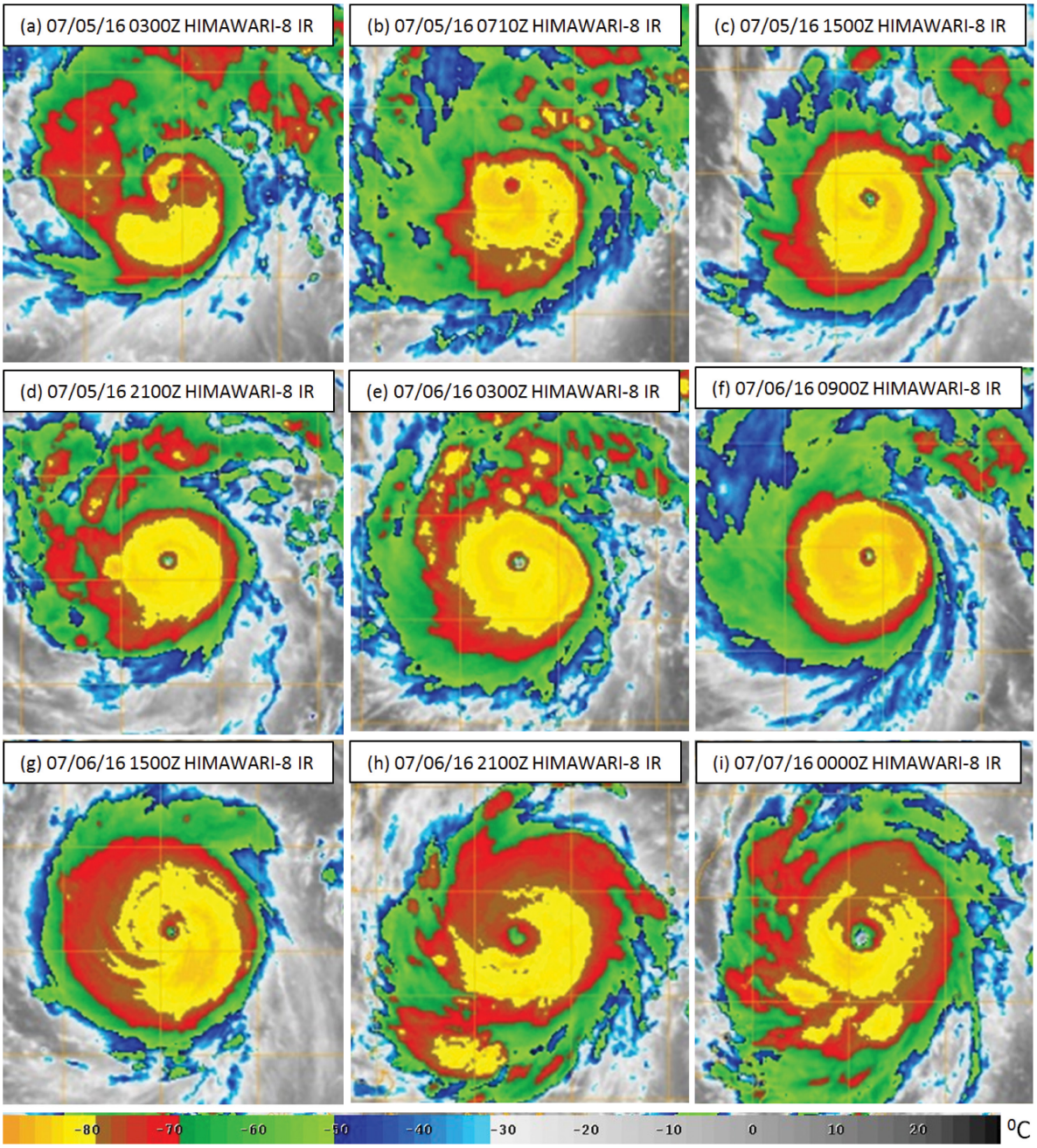

Fig. 10. Satellite Himawari-8 images of brightness temperature for Typhoon Nepartak at (a–d) 0300 UTC, 0710 UTC, 1500 UTC and 2100 UTC on 5 July, (e–h) 0300 UTC, 0900 UTC, 1500 UTC and 2100 UTC on 6 July, and (i) 0000 UTC 7 July 2016. Yellow lines mark latitudes/longitudes every 2 degrees.

the Himawari-8 satellite observations (Fig. 10). The cold and deep cloud top region (TB < −80°C) associated with the inner core is captured well by the model. More convective bands are found in the southern region with an asymmetric structure broadly apparent (Fig. 11). However, the synthetic TBs derived from the COAMPS-TC forecasts exhibit a much broader coverage of high cloud tops than the satellite observa-

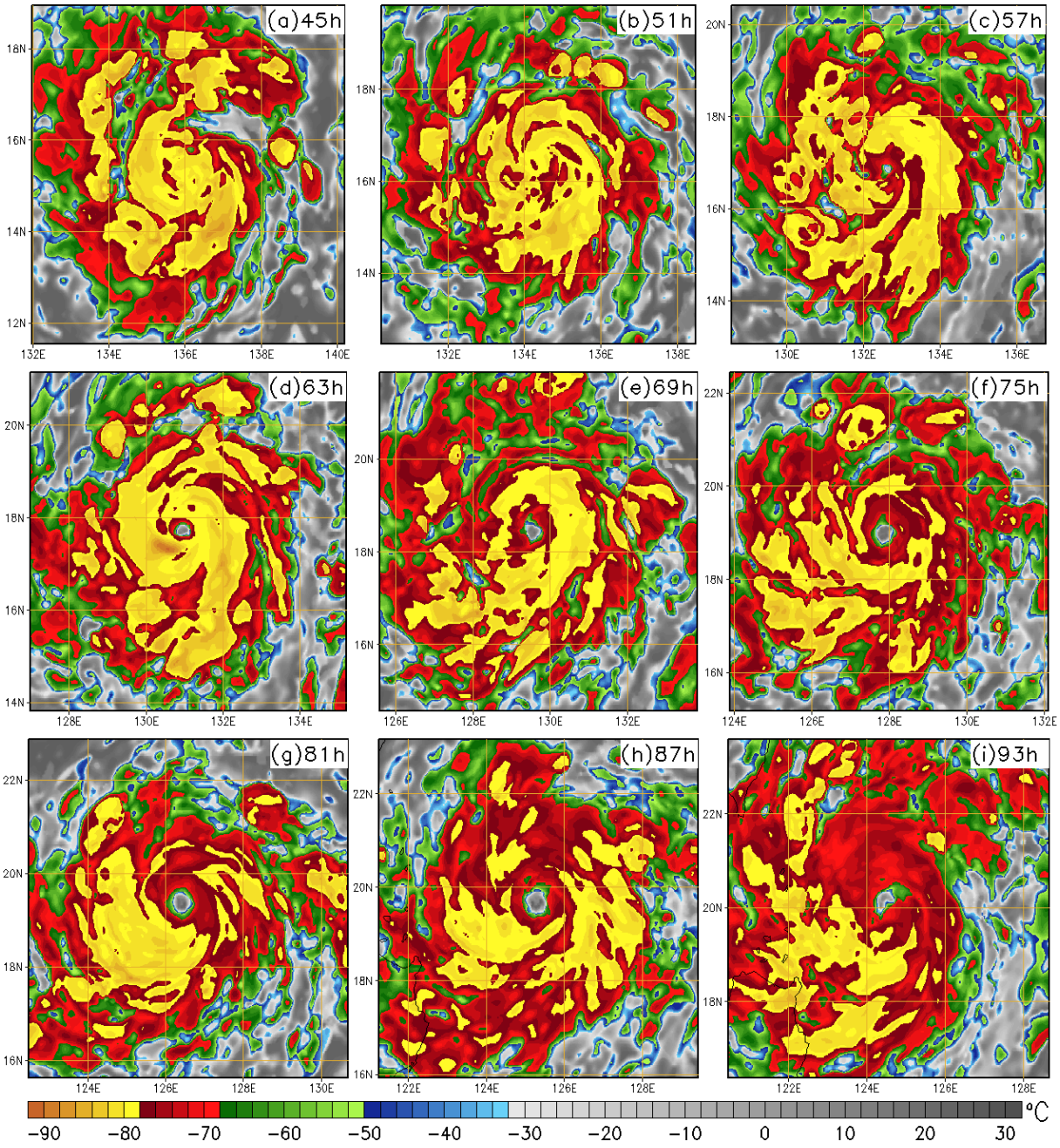

Fig. 11. Simulated brightness temperature (shaded, °C) of Typhoon Nepartak at (a–c) 45-h, 51-h, 57-h, (0900 UTC, 1500 UTC, 2100 UTC 5 July), (d–g) 63-h, 69-h, 75-h, 81-h, (0300 UTC, 0900 UTC, 1500 UTC, 2100 UTC 6 July), and (h–i) 87-h, 93-h (0300 UTC, 0900 UTC 7 July) from the forecast starting at 1200 UTC 3 July 2016. Yellow lines mark latitudes/longitudes every 2 degrees.

tions indicate. The simulated eye size (Figs. 11d–g) is ~ two times larger than the size apparent in the satellite imagery during the RI period (Fierro et al. 2009; Gentry and Lackmann 2010). The relative large simulated eye is also apparent in the azimuthally averaged fields (Fig. 4). The TC becomes more asymmetric during 69–93 h (Figs. 11e–i). One contributing factor to this discrepancy is that the model horizontal resolu-

tion (5 km) may not be high enough (Jin et al. 2014). A 5-km grid spacing used by the real-time COAMPS-TC during the 2016 season is not capable to capture the tight inner-core structure of Nepartak with a radius of just ~ 10 km. It should be noted that the resolution was increased in the operational version of COAMPS-TC to 4 km beginning in 2017.

5. Summary

Super Typhoon Nepartak was a category 5 tropical cyclone which had significant societal impacts. The real-time COAMPS-TC system produced reasonably accurate track and intensity forecasts for Nepartak and captured the RI phase as well. Our results suggest that the large-scale environment, particularly the upper-level divergence, lower-level convergence, weak vertical wind shear, ample moisture supply in lower levels (surface to 850-hPa), and warm SSTs (over 30°C) all set the stage for Nepartak's intensification. The surface enthalpy flux, and convective latent heat release act in concert to increase the TC primary and secondary circulations as RI ensues. The storm structure variations seen from the simulated TB during RI bear considerable resemblance to the observed satellite images from Himawari-8, although the forecast inner core is systematically too large relative to the satellite observations. Higher horizontal resolution is needed to improve the operational storm structure forecasts.

Acknowledgments

We thank the anonymous reviewers for their constructive comments. This research is supported by the Chief of Naval Research through the NRL Base Program, PE 0601153N, and the Office of Naval Research Tropical Cyclone Intensity DRI, PE 0601153N. We acknowledge computational support from a grant of High Performance Computing (HPC) time from the Navy Defense Resource Center (DSRC) at Stennis, MS. COAMPS-TC is a registered trademark of the Naval Research Laboratory.

References

Bikos, D., D. T. Lindsey, J. Otkin, J. Sieglaff, L. Grasso, C. Siewert, J. Correia, Jr., M. Coniglio, R. Rabin, J. S. Kain, and S. Dembek, 2012: Synthetic Satellite imagery for real-time high-resolution model evaluation. *Wea. Forecasting*, **27**, 784–795.

Bougeault, P., and P. Lacarrère, 1989: Parameterization of orography-induced turbulence in a mesobeta-scale model. *Mon. Wea. Rev.*, **117**, 1872–1890.

Central Emergency Operation Center, 2016: *Typhoon Nepartak report*. July 9, 2016.

China News Service, 2016: *Typhoon Nepartak report*. July 17, 2016.

Donelan, M. A., B. K. Haus, N. Reul, W. J. Plant, M. Stiassnie, H. C. Graber, O. B. Brown, and E. S. Saltzman, 2004: On the limiting aerodynamic roughness of the ocean in very strong winds. *Geophys. Res. Lett.*, **31**, L18306, doi:10.1029/2004GL019460.

Doyle, J. D., R. M. Hodur, S. Chen, Y. Jin, J. R. Moskaitis, S. Wang, E. A. Hendricks, H. Jin, and T. A. Smith, 2014: Tropical cyclone prediction using COAMPS-TC. *Oceanogr.*, **27**, 104–115.

Emanuel, K. A., 1986: An air-sea interaction theory for tropical cyclones. Part I: Steady-state maintenance. *J. Atmos. Sci.*, **43**, 585–604.

Emanuel, K. A., 1994: *Atmospheric Convection*. Oxford University Press, 580 pp.

Emanuel, K. A., 2003: Tropical cyclones. *Ann. Rev. Earth Planet. Sci.*, **31**, 75–104.

ESCAP/WMO Typhoon Committee, 2017: Report on TC's key activities and main events in the region (WRD/TC.49/6.1). *49th Session of ESCAP/WMO Typhoon Committee*, February 2017, Yokohama, Japan.

Fierro, A. O., R. F. Rogers, F. D. Marks, and D. S. Nolan, 2009: The impact of horizontal grid spacing on the microphysical and kinematic structures of strong tropical cyclones simulated with the WRF-ARW Model. *Mon. Wea. Rev.*, **137**, 3717–3743.

Fu, Q., and K. N. Liou, 1993: Parameterization of the radiative properties of cirrus clouds. *J. Atmos. Sci.*, **50**, 2008–2025.

Gentry, M. S., and G. M. Lackmann, 2010: Sensitivity of simulated tropical cyclone structure and intensity to horizontal resolution. *Mon. Wea. Rev.*, **138**, 688–704.

Holiday, C. R., and A. H. Thompson, 1979: Climatological characteristics of rapidly intensifying typhoons. *Mon. Wea. Rev.*, **107**, 1022–1034.

Jin, H., M. S. Peng, Y. Jin, and J. D. Doyle, 2014: An evaluation of the impact of horizontal resolution on tropical cyclone predictions using COAMPS-TC. *Wea. Forecasting*, **29**, 252–270.

Jin, Y., W. T. Thompson, S. Wang, and C.-S. Liou, 2007: A numerical study of the effect of dissipative heating on tropical cyclone intensity. *Wea. Forecasting*, **22**, 950–966.

Jin, Y., S. Wang, J. Nachamkin, J. D. Doyle, G. Thompson, L. Grasso, T. Holt, J. Moskaitis, H. Jin, R. M. Hodur, Q. Zhao, M. Liu, and M. DeMaria, 2014: The impact of ice phase cloud parameterizations on tropical cyclone prediction. *Mon. Wea. Rev.*, **142**, 606–625.

Kanada, S., S. Tsujino, H. Aiki, M. K. Yoshisoka, Y. Miyazawa, K. Tsuboki, and I. Takayabu, 2017: Impacts of SST patterns on rapid intensification of Typhoon Megi (2010). *J. Geophys. Res.*, **122**, 13245–13262.

Kaplan, J., and M. DeMaria, 2003: Large-scale characteristics of rapidly intensifying tropical cyclones in the

North Atlantic basin. *Wea. Forecasting*, **18**, 1093–1108.

Kaplan, J., M. DeMaria, and J. A. Knaff, 2010: A revised tropical cyclone rapid intensification index for the Atlantic and eastern North Pacific basins. *Wea. Forecasting*, **25**, 220–241.

Kondo, J., 1975: Air-sea bulk transfer coefficients in diabatic conditions. *Bound.-Layer Meteor.*, **9**, 91–112.

Liu, M., J. E. Nachamkin, and D. L. Westphal, 2009: On the improvement of COAMPS weather forecasts using an advanced radiative transfer model. *Wea. Forecasting*, **24**, 286–306.

Marchok, T. P., 2002: How the NCEP tropical cyclone tracker works. *25th Conf. Hurr. Trop. Meteor.*, San Deigo, CA, Amer. Meteor. Soc., 21–22 [Available at https://ams.confex.com/ams/pdfpapers/37628.pdf.].

Mellor, G. L., and T. Yamada, 1974: A hierarchy of turbulence closure models for planetary boundary layers. *J. Atmos. Sci.*, **31**, 1791–1806.

Merrill, R. T., 1988: Environmental influences on hurricane intensification. *J. Atmos. Sci.*, **45**, 1678–1687.

Montgomery, M. T., and R. K. Smith, 2014: Paradigms for tropical-cyclone intensification. *Aust. Meteor. Oceanogr. J.*, **64**, 37–66.

Rutledge, S. A., and P. V. Hobbs, 1984: The mesoscale and microscale structure and organization of clouds and precipitation in mildlatitude cyclones. XII: A diagnostic modeling study of precipitation development in narrow cold-frontal rainbands. *J. Atmos. Sci.*, **41**, 2949–2972.

Soloviev, A. V., R. Lukas, M. A. Donelan, B. K. Haus, and I. Ginis, 2014: The air-sea interface and surface stress under tropical cyclones. *Sci. Rep.*, **4**, 5306, doi: 10.1038/srep05306.

Stern, D. P., J. Vigh, D. Nolan, and F. Zhang, 2015: Revisiting the relationship between eyewall contraction and intensification. *J. Atmos. Sci.*, **72**, 1283–1306.